Unsteady Euler Algorithm with Unstructured Dynamic Mesh for Complex-Aircraft Aerodynamic Analysis

John T. Batina*
NASA Langley Research Center, Hampton, Virginia 23665

An Euler solution algorithm is presented for unsteady aerodynamic analysis of complex-aircraft configurations. The flow solver involves a multistage Runge-Kutta time-stepping scheme that uses a finite-volume spatial discretization on an unstructured grid made up of tetrahedra. A significant contribution of the research is the development and implementation of a moving mesh algorithm that is employed for problems involving static or dynamic deformation of the aircraft. The mesh algorithm is a general procedure that can treat realistic motions and deformations of complex-aircraft configurations. Steady and unsteady results are presented for a supersonic fighter configuration to demonstrate applications of the Euler solver and dynamic mesh algorithm. The unsteady flow results were obtained for the aircraft oscillating harmonically in a complete-vehicle bending mode. Effects of angle of attack and reduced frequency on instantaneous pressures and force responses were investigated. The paper presents descriptions of the Euler solver and dynamic mesh algorithm along with results that assess the capability.

Introduction

CONSIDERABLE progress has been made over the past two decades on developing computational fluid dynamics (CFD) methods for aerodynamic analysis.[1,2] Recent work in CFD has focused primarily on developing algorithms for the solution of the Euler and Navier-Stokes equations. This work has centered largely on developing methods of solution that assume that the computational grid has an underlying geometrical structure. It is generally recognized, however, that it is difficult to generate a structured grid about complex-aircraft configurations. A blocked grid or zonal-type approach[3,4] has helped to alleviate the problem with structured grids for complex-aircraft applications, but the grid generation task is still formidable, and significant algorithm modifications to existing single-block flow solvers need to be made to accommodate multiblock grids. Furthermore, this difficulty is magnified when the aeroelastic deformation of the aircraft is considered, since the grid must move to conform to the instantaneous shape of the vehicle. As an alternative, algorithms have been developed recently that make use of unstructured grids.[5-12] In two dimensions, these grids typically are made up of triangles, and in three dimensions, they consist of an assemblage of tetrahedra. These triangles or tetrahedra are oriented to conform to the geometry being considered, thus making the treatment of complicated shapes possible. For a complex-aircraft configuration, a tetrahedral grid can be generated about the entire geometry in a single application of the grid generation program. In contrast, a structured grid about the aircraft is usually constructed by first breaking up the problem into a number of simpler shapes that are easier to grid and then assembling these grids to form the total mesh about the aircraft.

The unstructured grid methods, therefore, have the distinct advantage over structured grid methods in that they can easily treat complex geometric configurations as well as complicated flow physics. For example, an inviscid transonic flow solution was presented by Jameson et al.[7] for the Boeing 747 aircraft that was computed using an unstructured tetrahedral grid. In this calculation, the complete-vehicle geometry was modeled including multiple lifting surfaces, the fuselage, underwing pylons, and flow-through engine nacelles. Furthermore, the unstructured grid flow solvers easily lend themselves to solution adaptive procedures where the grid is adapted to gradients of the solution to more accurately resolve the flow physics. As discussed by Lohner,[9] this may be accomplished using mesh movement, mesh enrichment, or remeshing, all of which pose no problems for most unstructured grid flow solvers. In contrast, a structured grid flow solver becomes relatively much more complicated when refinement procedures, such as embedded grids, are utilized.

An assessment of the applicability of the unstructured grid methodology for unsteady aerodynamic analysis for airfoils was reported by the author in Ref. 12. Calculations were performed using a newly developed Euler code for the two-dimensional time-dependent flow about oscillating airfoils using an unstructured grid made up of triangles. A dynamic mesh algorithm was also employed for problems involving airfoil motion. In Ref. 12, it was shown that the unsteady results obtained using the unstructured grid were comparable to three dimensional configurations. It was concluded that the advantages of the unstructured grid methodology are very attractive for unsteady aerodynamic and aeroelastic analysis of three-dimensional configurations. Therefore, effort was directed toward developing an Euler solver for unsteady aerodynamic analysis of complete-aircraft configurations. The purpose of this paper is to describe this development effort and to report on the results of applications of the new computer code. The solver is similar to the multistage Runge-Kutta time-stepping scheme of Ref. 5, which uses a finite-volume spatial discretization on an unstructured grid made up of tetrahedra. A significant contribution of the present research is the development and implementation of a moving mesh algorithm that is employed for problems involving static or dynamic deformation of the aircraft. The mesh algorithm is a general procedure that can treat realistic motions and deformations of complex-aircraft configurations. One of the objectives of the study was to investigate the applicability of the unstructured grid methodology for three-dimensional time-dependent problems with moving boundaries. The eventual application is for aeroelastic analysis, with the Euler or Navier-Stokes equations, of aircraft configurations involving a high degree of geometrical complexity. As such, the present work is a significant step toward achieving this goal. The paper presents descriptions of

Received May 8, 1989; revision received Feb. 16, 1990.

*Senior Research Scientist, Unsteady Aerodynamics Branch, Structural Dynamics Division. Senior Member AIAA.

the Euler solver and dynamic mesh algorithm along with results that assess the capability.

Euler Equations

In the present study, the flow is assumed to be governed by the three-dimensional time-dependent Euler equations, which may be written in integral form as

$$\frac{\partial}{\partial t}\int_{\Omega} \boldsymbol{Q}\,\mathrm{d}V + \int_{\partial\Omega} (\boldsymbol{F}\,\mathrm{d}A_x + \boldsymbol{G}\,\mathrm{d}A_y + \boldsymbol{H}\,\mathrm{d}A_z) = 0 \qquad (1)$$

where the vector of conserved variables $\boldsymbol{Q}$ and the convective fluxes $\boldsymbol{F}$, $\boldsymbol{G}$, and $\boldsymbol{H}$ are given by

$$\boldsymbol{Q} = \begin{bmatrix} \rho \\ \rho u \\ \rho v \\ \rho w \\ e \end{bmatrix} \qquad (2a)$$

$$F = \begin{bmatrix} \rho U \\ \rho U u + p \\ \rho U v \\ \rho U w \\ (e + p)U + x_t p \end{bmatrix} \qquad (2b)$$

$$G = \begin{bmatrix} \rho V \\ \rho V u \\ \rho V v + p \\ \rho V w \\ (e + p)\ V + y_t p \end{bmatrix} \qquad (2c)$$

$$H = \begin{bmatrix} \rho W \\ \rho W u \\ \rho W v \\ \rho W w + p \\ (e + p)\ W + z_t p \end{bmatrix} \qquad (2d)$$

The contravariant velocities, U, V, and W are defined by

$$U = u - x_t, \qquad V = v - y_t \qquad W = w - z_t \qquad (3)$$

where x_t, y_t, and z_t are the grid speeds in the x, y, and z directions, respectively, and the pressure p is given by the equation of state for a perfect gas

$$p = (\gamma - 1)\left[e - \frac{1}{2}\rho\,(u^2 + v^2 + w^2)\right] \qquad (4)$$

These equations have been nondimensionalized by the freestream density ρ_∞ and the freestream speed of sound a_∞.

Solution Algorithm

In this section, an algorithm is presented for the solution of the three-dimensional time-dependent Euler equations that reduces conceptually to central differencing on a rectangular mesh.

Spatial Discretization

The Euler equations in integral form [Eq. (1)] are solved using a finite-volume algorithm that was developed for analysis with an unstructured grid made up of tetrahedra. The algorithm is a nodal scheme whereby the flow variables are stored at the vertices of the tetrahedra that have a vertex at that node. The boundary integral in Eq. (1) is approximated as follows. First, along each face of the control volume boundary, the fluxes at the three vertices are averaged. Then, the contribution to the boundary integral is determined by taking the product of the averaged fluxes with the directed area of the face, as shown in Fig. 1. Along the face defined by nodes 1, 2, and 3, for example, the contribution to the boundary integral in Eq. (1) is given by

$$1/3\ (\boldsymbol{F}_1 + \boldsymbol{F}_2 + \boldsymbol{F}_3)A_x + 1/3\ (\boldsymbol{G}_1 + \boldsymbol{G}_2 + \boldsymbol{G}_3)Ay + 1/3\ (\boldsymbol{H}_1 + \boldsymbol{H}_2 + \boldsymbol{H}_3)A_z$$

The algorithm identically conserves mass, momentum, and energy because the flux through the face 1-2-3, which is out of the control volume centered at node 4, is equal to the flux into the control volume centered at node 5.

Artificial Dissipation

The unsteady Euler equations are a set nondissipative hyperbolic conservation laws whose numerical solution requires some form of artificial dissipation to prevent oscillations near shock waves and to damp high-frequency uncoupled error modes. On structured meshes, an adaptive blend of second and fourth differences of the conserved variables has been shown to be an effective form of dissipation.[13] In the present unstructured mesh Euler solver, a combination of harmonic and biharmonic operators is employed, corresponding to second and fourth differences, respectively. Similar to that of Jameson and co-workers,[5-7] the biharmonic operator provides a background dissipation to damp high-frequency errors, and the harmonic operator prevents oscillations near shocks. The harmonic operator is multiplied by a pressure switch that is first-order accurate near shocks and is second-order accurate in smooth regions of the flow. The biharmonic operator is third-order accurate and is adaptively turned off to prevent overshoots in regions of shock waves.

Time Integration

The Euler equations are integrated in time by assuming that the conserved variables represented by $\boldsymbol{Q}$ are constant within a control volume that yields

$$\frac{\mathrm{d}}{\mathrm{d}t}(V_i\,\boldsymbol{Q}_i) + C(\boldsymbol{Q}) - D(\boldsymbol{Q}) = 0 \qquad (5)$$

where C and D are the convective and dissipative operators, respectively, and V_i is the volume of the control volume surrounding node i. These equations are integrated in time using an explicit four-stage Runge-Kutta time-stepping scheme given by

$$\boldsymbol{Q}^{(0)} = \boldsymbol{Q}^n \qquad (6a)$$

$$\boldsymbol{Q}^{(1)} = \frac{V^n}{V^{n+1}}\,\boldsymbol{Q}^{(0)} - \frac{1}{4}\frac{\Delta t}{V^{n+1}}\,[C(\boldsymbol{Q}^{(0)}) - D(\boldsymbol{Q}^{(0)})] \qquad (6b)$$

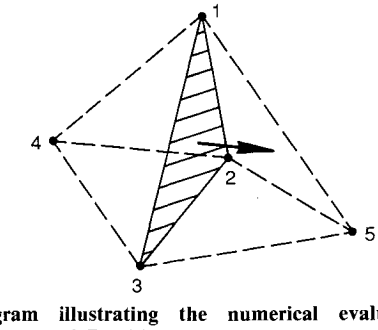

Fig. 1 Diagram illustrating the numerical evaluation of the boundary integral of Eq. (1).

$$Q^{(2)} = \frac{V^n}{V^{n+1}} Q^{(0)} - \frac{1}{3} \frac{\Delta t}{V^{n+1}} [C(Q^{(1)}) - D(Q^{(0)})] \quad (6c)$$

$$Q^{(3)} = \frac{V^n}{V^{n+1}} Q^{(0)} - \frac{1}{2} \frac{\Delta t}{V^{n+1}} [C(Q^{(2)}) - D(Q(0))] \quad (6d)$$

$$Q^{(4)} = \frac{V^n}{V^{n+1}} Q^{(0)} - \frac{\Delta t}{V^{n+1}} [C(Q^{(3)}) - D(Q^{(0)})] \quad (6e)$$

$$Q^{n+1} = Q^{(4)} \quad (6f)$$

In this scheme, the convective operator is evaluated at each stage and, for computational efficiency, the dissipative operator is evaluated only at the first stage. The Runge-Kutta scheme represented by Eqs. (6a–f) is second-order accurate in time and includes the necessary terms to account for changes in cell volumes due to a moving or deforming mesh.

Implicit Residual Smoothing

The explicit time-integration scheme described in the previous section has a step size that is limited by the Courant-Friedricks-Lewy (CFL) condition corresponding to a CFL number of $2\sqrt{2}$. To accelerate convergence to steady state, the CFL number may be increased by averaging the residual R_i with values at neighboring grid points. This is accomplished by replacing R_i by the smoothed residual $\bar{R}_i$ given by

$$\bar{R}_i - \epsilon \nabla^2 \bar{R}_i = R_i \quad (7)$$

where ϵ is a constant that controls the amount of smoothing and ∇^2 is an undivided Laplacian operator. These implicit equations are solved approximately using several Jacobi iterations similar to what is done in Refs. 5 and 6.

Convergence to steady state is further accelerated using enthalpy damping[13] and local time stepping. The local time stepping uses the maximum allowable step size at each grid point as determined by a local stability analysis. For unsteady applications, however, a global time step must be used because of the time-accuracy requirement. The maximum allowable global time step may be increased to a value that is larger than that dictated by the CFL condition by using a time-accurate version of Eq. (7) similar to that of Ref. 14. In this procedure, the constant ϵ is replaced by a parameter that varies from grid point to grid point, which is defined by

$$\epsilon = \max \left[\frac{1}{4} \left(\frac{\Delta t^2}{\Delta t^2_{\text{CFL}}} - 1 \right), 0.0 \right] \quad (8)$$

In Eq. (8), Δt is the time step taken and Δt_{CFL} is the local allowable time step for the four-stage Runge-Kutta time-stepping scheme.

Boundary Conditions

To impose the no-flow-through boundary condition along the surface of the aircraft, the boundary integral of Eq. (1) is first rewritten in terms of the flux velocity defined by $UA_x + VA_y + WA_z$. Then, for control volumes with faces along the aircraft surface, the flux velocity along these faces, which is proportional to the velocity normal to the face, is set equal to zero.

In the far field, a characteristic analysis based on Riemann invariants is used to determine the values of the flow variables on the outer boundary of the grid. This analysis correctly accounts for wave propagation in the far field, which is important for rapid convergence to steady state and serves as a "nonreflecting" boundary condition for unsteady applications.

Dynamic Mesh Algorithm

A significant contribution of the present research is the development and implementation of a dynamic mesh algorithm that is employed for problems where the aircraft deforms. The original mesh corresponding to the undeformed vehicle is moved to conform to the instantaneous shape of the vehicle by modeling each edge of each tetrahedron by a spring. The spring stiffness for a given edge $i-j$ is taken to be inversely proportional to the length of the edge as

$$k_m = 1/[(x_j - x_i)^2 + (y_j - y_i)^2 + (z_j - z_i)^2]^{1/2} \quad (9)$$

Grid points on the outer boundary of the mesh are held fixed and the instantaneous location of the points of the inner boundary (aircraft) are given by the prescribed surface motion. At each time step, the static equilibrium equations in the x, y, and z directions, which result from a summation of forces, are solved iteratively at each interior node i of the grid for the displacements δ_{x_i}, δ_{y_i}, and δ_{z_i}. This is accomplished by using a predictor-corrector procedure, which first predicts the displacements of the nodes by extrapolation from grids at previous time levels according to

$$\bar{\delta}_{x_i} = 2\,\delta^n_{x_i} - \delta^{n-1}_{x_i}, \quad \bar{\delta}_{y_i} = 2\,\delta^n_{y_i} - \delta^{n-1}_{y_i}, \quad \bar{\delta}_{z_i} = 2\,\delta^n_{z_i} - \delta^{n-1}_{z_i} \quad (10)$$

and then corrects these displacements using several Jacobi iterations of the static equilibrium equations using

$$\delta^{n+1}_{x_i} = \frac{\Sigma\, k_m\, \bar{\delta}_{x_m}}{\Sigma\, k_m}, \quad \delta^{n+1}_{y_i} = \frac{\Sigma\, k_m\, \bar{\delta}_{y_m}}{\Sigma\, k_m}, \quad \delta^{n+1}_{z_i} = \frac{\Sigma\, k_m\, \bar{\delta}_{z_m}}{\Sigma\, k_m} \quad (11)$$

In Eqs. (11), the summations are performed over all of the edges of the tetrahedra that make up the control volume of node i. The new locations of the interior nodes are then determined by

$$x^{n+1}_i = x^n_i + \delta^{n+1}_{x_i}, \quad y^{n+1}_i = y^n_i + \delta^{n+1}_{y_i}, \quad z^{n+1}_i = z^n_i + \delta^{n+1}_{z_i} \quad (12)$$

The predictor-corrector procedure has been found to be more efficient than simply performing Jacobi iterations because far fewer iterations are required to achieve acceptable convergence. In practice, it has been found that only one or two iterations are sufficient to move the mesh accurately. As an example of how the mesh moves, a coarse grid for the Pathfinder 1 configuration at $\alpha = 0$ deg was obtained with the resulting surface triangulation shown in Fig. 2. The total grid has 21,809 nodes and 119, 884 tetrahedra. For the example considered here, the aircraft was oscillated in a pitching mode for one cycle of sinusoidal motion with an amplitude of 15 deg. The instantaneous meshes obtained using Eqs. (10–12) at the maximum and minimum pitch angles are shown in Figs. 3a and 3b, respectively. The mesh moves smoothly as the aircraft pitches, and the procedure is completely general in that it can treat realistic motions and deformations of complex-aircraft configurations.

Geometric Conservation Law

To avoid errors induced by the moving mesh, a geometric conservation law needs to be satisfied numerically, in addition to the mass, momenta, and energy conservation laws that

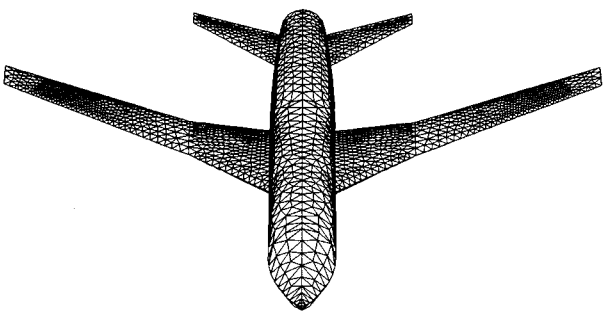

Fig. 2 Surface triangulation for the Pathfinder 1 configuration.

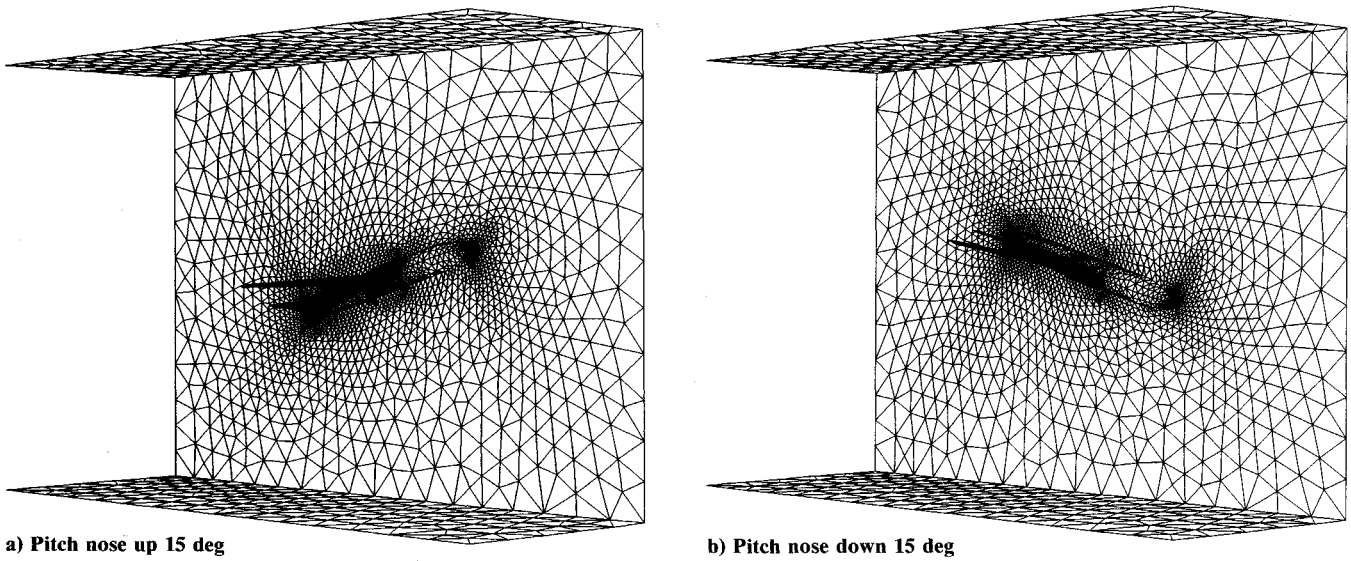

a) Pitch nose up 15 deg

b) Pitch nose down 15 deg

Fig. 3 Surface triangulation for the Pathfinder 1 configuration and grid boundaries that illustrate how the mesh moves for a pitching airplane.

govern the physics of the flow. In most of the unsteady flow computations on moving meshes that have been pubished previously, however, this additional conservation law has not been satisfied. As discussed by Thomas and Lombard,[15] the geometric conservation law is of the same integral form as the mass conservation law and is defined by

$$\frac{\partial}{\partial t}\int_{\Omega} dV + \int_{\partial\Omega} (x_t A_x + y_t A_y + z_t A_z) = 0 \qquad (13)$$

This geometric conservation law must be solved numerically using the same scheme that is used to integrate the conservation laws of the fluid to provide a self-consistent solution for the local cell volumes.[15] Discretization of Eq. (13), consistent with the solution algorithm already presented, yields

$$V_i^{n+1} = V_i^n + \Delta t \sum (x_{t_m}^{n+1} A_x + y_{t_m}^{n+1} A_y + z_{t_m}^{n+1} A_z) \qquad (14)$$

where the summation is taken over all edges of the control volume with endpoints at node i.

It is easy to demonstrate that the addition of the geometric conservation law is important for computations involving moving meshes by considering a uniform steady-state flow. Conservative finite-volume schemes with a fixed mesh have the property that a uniform flow is an exact solution of the numerical algorithm. For a moving mesh, the uniform flow is preserved only if the cell volumes are computed using the discrete form of the geometric conservation law. This is true even if the mesh moves rigidly and the cell volumes are not changing geometrically. Similarly, for nonuniform flows, the cell volumes need to be recomputed at each time step for rigidly moving meshes or for deforming meshes to prevent grid-motion induced errors in the numerical solution. Therefore, Eq. (14) was used in the present study to compute the local cell volumes at time level $(n + 1)$, as required by the time-integration scheme of Eqs. (6a–f).

Programming Considerations

Flow solvers based on unstructured grids have additional programming considerations that are not necessary in solvers based on structured grids. For example, connectivity information is required to determine which nodes make up a given tetrahedron and an indirect addressing system is used to access this information. Furthermore, special programming strategies that make extensive use of gather and scatter operations

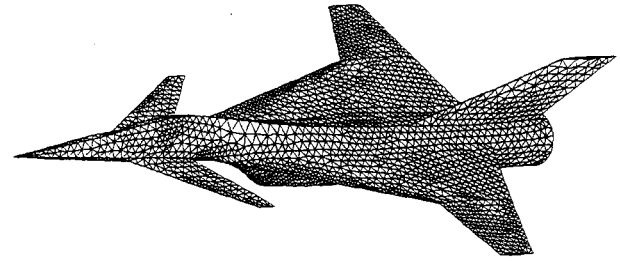

Fig. 4 Surface triangulation for the Langley fighter configuration.

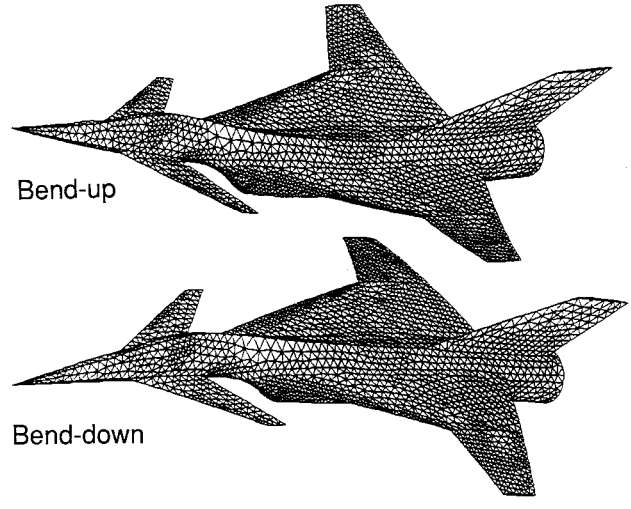

Fig. 5 Surface triangulation for the Langley fighter configuration illustrating an assumed complete-vehicle bending mode.

are used to achieve full vectorization of the solution algorithm.[16] Vectorization is accomplished primarily by sorting the elements into groups, such that, within each group, no element accesses the same node. This avoids vector recurrences in the flux balance computation, which would prevent vectorization. The programming procedure then "gathers" flow variable information from the elements into these groups, performs the flux balance separately within each group to solve the Euler equations, and finally "scatters" the resulting information back to the nodes that make up the grid.

Results and Discussion

To assess the Euler solver and dynamic mesh algorithm, calculations were performed for a supersonic fighter configu-

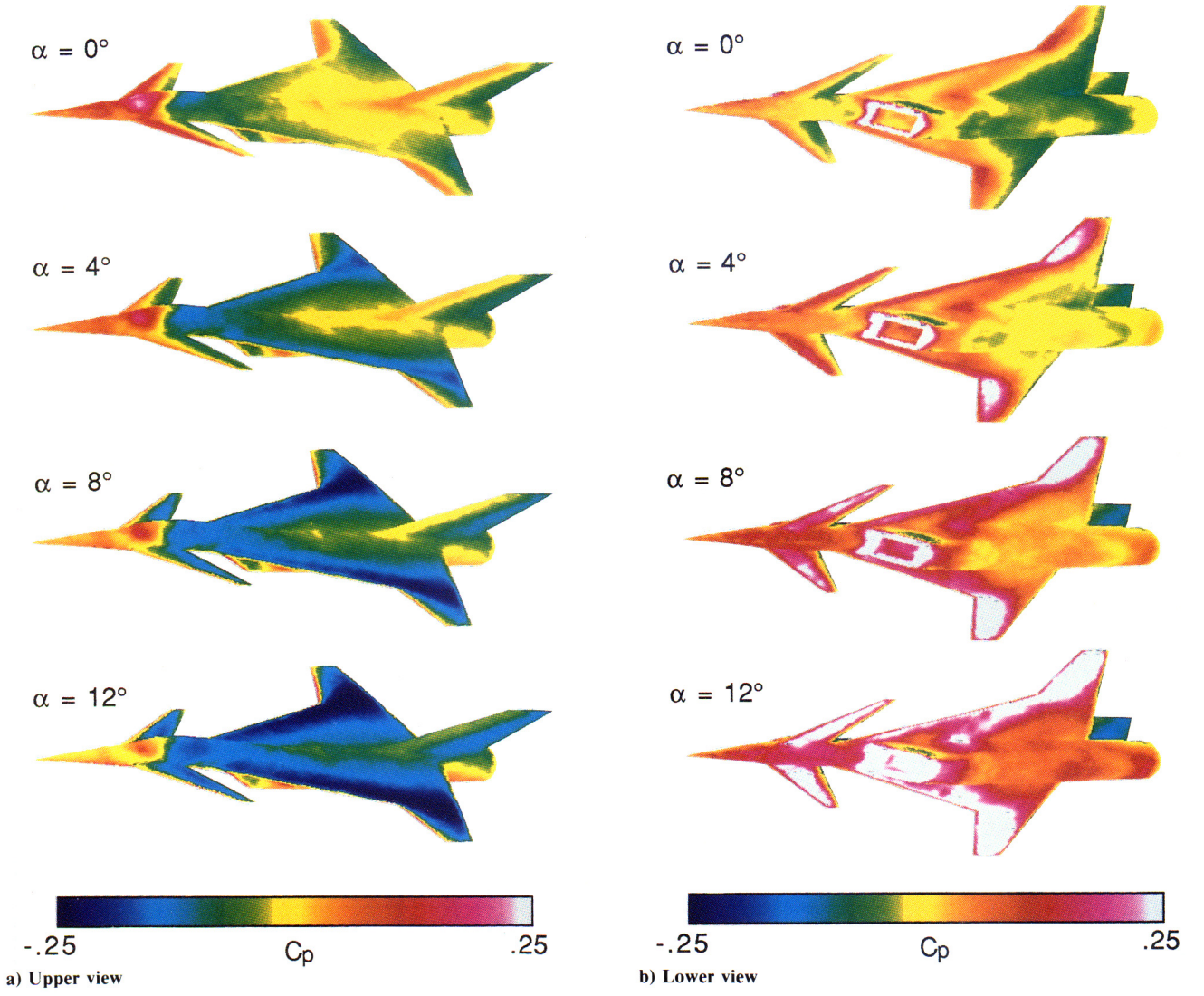

Fig. 6 Steady pressure coefficient contours on the Langley fighter configuration at $M_\infty = 2.0$.

ration that was tested at NASA Langley Research Center. The fighter will hereafter be referred to as the Langley fighter.[17] The Langley fighter is an aircraft designed to cruise at supersonic Mach numbers and also to maneuver efficiently at transonic speeds. The aircraft has a high-fineness ratio fuselage with an underslung swept inlet and a flow-through duct. Other components that make up the configuration include a cranked wing with a leading-edge sweep of 70 deg inboard and 20 deg outboard, a 55 deg swept canard, and a 60 deg swept vertical tail. All of the lifting surfaces have thin circular-arc airfoil sections. Results were obtained for the Langley fighter using a grid that has 13,832 nodes and 70,125 tetrahedra. The surface triangulation of the aircraft is shown in Fig. 4. Because of symmetry, the calculations were performed for only half of the aircraft, which contained 4581 triangles on the surface of the vehicle. Steady-state results were obtained for the Langley fighter at a freestream Mach number of $M_\infty = 2.0$ and four angles of attack including $\alpha = 0$, 4, 8, and 12 deg. Unsteady results were obtained at $\alpha = 0$ and 12 deg for the aircraft oscillating harmonically in an assumed polynomial complete-vehicle bending mode, which is shown in Fig. 5. Three values of reduced frequency based on wingtip semichord were considered including $k = 0.025$, 0.05, and 0.1. The amplitude of the deformation was taken to be one-fifth of the mode shape shown in the figure. So, for example, the wingtip deflection in the calculation was approximately 20% of the tip chord. The unsteady results are presented as instantaneous pressure coefficient contours on the vehicle surface and force coefficient responses.

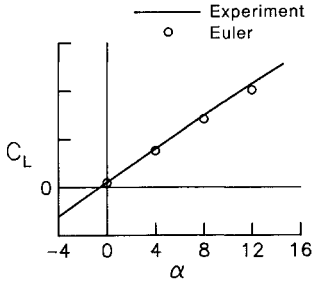

Fig. 7 Comparison between calculated and experimental lift coefficient vs angle of attack for the Langley fighter at $M_\infty = 2.0$.

Steady Flow Results

Steady flow results were obtained for the Langley fighter configuration using 1500 iterations starting from freestream flow conditions. Convergence to steady state was accelerated using local time stepping, implicit residual smoothing, and enthalpy damping. In each case, the error in the solution, as defined by the L_2 norm of the density residual, was reduced by approximately four orders of magnitude. The resulting steady pressure coefficient contours on the surface of the vehicle are shown in Figs. 6. Contours on the upper part of the aircraft are shown in Fig. 6a and contours on the lower part of the aircraft are shown in Fig. 6b. On the upper part of the aircraft (Fig. 6a), the pressures generally indicate flow compression (red-white contours) on the forward part of the aircraft nose,

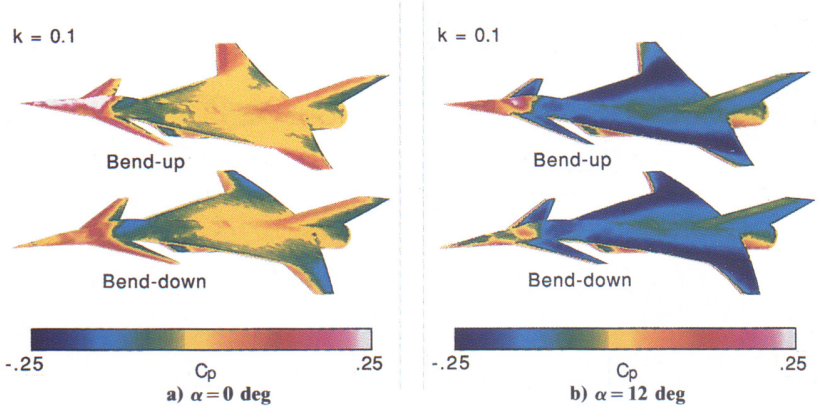

Fig. 8 Effects of angle of attack on instantaneous pressure coefficient contours on the Langley fighter configuration at the maximum (bend-up) and minimum (bend-down) amplitudes of deformation at $M_\infty = 2.0$.

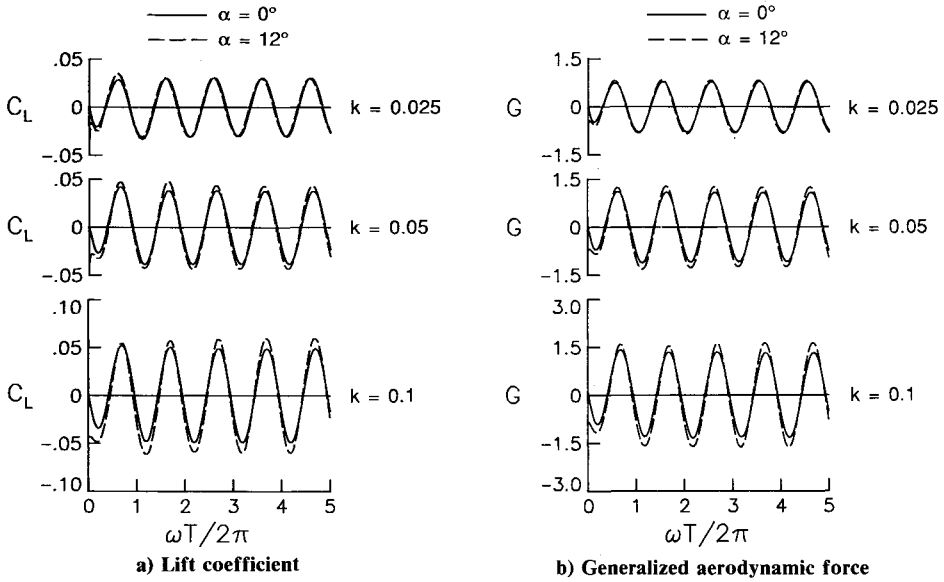

Fig. 9 Effects of angle of attack and reduced frequency on force coefficient responses due to complete-vehicle sinusoidal bending deformation of the Langley fighter configuration at $M_\infty = 2.0$.

canopy, and canards with expansion on the downstream part of the canopy (green-blue contours). The aft outboard regions of the cranked wing and the vertical tail show similar flow features with compression along the leading edges and expansion along the trailing edges, which is expected for supersonic flow. As the angle of attack is increased, the flow compression on the forward canopy decreases and the levels of flow expansion increase significantly on a large portion of the upper surfaces of the vehicle. This is especially true aft of the canopy, near the trailing edges of the canards and vertical tail, and near the inboard leading edges of the wings. The highest levels of flow expansion occur at $\alpha = 12$ deg near the inboard leading edges of the wings extending onto the aft outboard regions. This is due to flow separation along the inboard part of the leading edges caused by the sharp edges and the relatively high angle of attack and Mach number. The vortex that is produced is indicated by the dark blue contouring in the figure.

On the lower part of the aircraft (Fig. 6b), there is a considerable amount of flow compression, which increases significantly as the angle of attack increases. For example, there is a strong highly-swept shock wave beneath the aircraft that impinges on the edges of the inlet as indicated there by the white contours. As the angle of attack is increased, this shock becomes stronger, as indicated by the increased size of the white area at the inlet. The flow compression also increases on the underside of the canards and the outboard regions of the wing.

A comparison between calculated and experimental lift coefficient vs angle of attack for the Langley fighter is shown in Fig. 7. In general, the calculated lift coefficient agrees well with the experimental data, especially at the lower angles of attack of 0 and 4 deg. At the higher angles of attack of 8 and 12 deg, the calculated lift is slightly underpredicted in comparison with the measured values, which is possibly due to the coarseness of the grid.

Unsteady Flow Results

Unsteady flow results were obtained for the Langley fighter configuration oscillating harmonically in a complete-vehicle bending mode. The calculations were performed for $k = 0.025$, 0.05, and 0.1 using 1440, 720, and 360 steps per cycle of motion, respectively, for five cycles. Calculated instantaneous pressure contours at the maximum (bend-up) and minimum (bend-down) amplitudes of oscillation, during the fifth cycle, for $k = 0.1$ are shown in Figs. 8. Pressure contours at $\alpha = 0$ deg are shown in Fig. 8a; pressure contours at $\alpha = 12$ deg are shown in Fig. 8b. During the first half of the cycle (bend-up) at $\alpha = 0$ deg, the level of flow compression increases along the nose, the forward canopy of the vehicle, and near the leading edge of the outboard part of the wings. During the latter half of the cycle (bend-down) at $\alpha = 0$ deg, the level of flow expansion increases near the trailing edge of the wings and on the aft canopy region. At $\alpha = 12$ deg (Fig. 8b), the changes in pressure are very similar to those at $\alpha = 0$ deg. For example, during the first half of the cycle, the flow compres-

sion increases along the forward canopy, and during the latter half of the cycle, the opposite situation occurs and the flow expansion increases near the trailing edges of the wings.

To quantify the effects of angle of attack and reduced frequency, force coefficient responses for the Langley fighter oscillating in the complete-vehicle bending mode at $M_\infty = 2.0$ are presented in Figs. 9. Five cycles of motion were considered as plotted. The aircraft lift coefficient C_L is shown in Fig. 9a, and the generalized aerodynamic force G is shown in Fig. 9b. The generalized aerodynamic force, used in aeroelastic and flutter analyses, is defined as the pressure induced by the oscillatory motion multiplied by the mode shape, which is integrated over the surface of the vehicle. For both the lift coefficient and the generalized aerodynamic force, the mean values of the oscillating loads were subtracted off to allow for a direct comparison between results obtained at $\alpha = 0$ and 12 deg. As shown in Figs. 9, the effects of angle of attack are very small for $k = 0.025$ and the generalized aerodynamic force is very similar to the lift coefficient. As the reduced frequency is increased, however, the magnitudes of the response of the aircraft increase and there is a small change in phase of approximately 35 deg in both the lift and the generalized force. Also, an effect due to angle of attack becomes evident, in that the responses at $\alpha = 12$ deg are of larger magnitude than those at $\alpha = 0$ deg. This effect is possibly attributable to the small amount of vortical flow that is present along the upper surface of the wings in the inboard region at $\alpha = 12$ deg.

Concluding Remarks

An Euler solution algorithm was presented for unsteady aerodynamic analysis of complex-aircraft configurations. The flow solver involves a multistage Runge-Kutta time-stepping scheme that uses a finite-volume spatial discretization on an unstructured grid made up of tetrahedra. A significant contribution of the research was the development and implementation of a moving mesh algorithm that is employed for problems involving static or dynamic deformation of the aircraft. The mesh algorithm is a general procedure that can treat realistic motions and deformations of complex-aircraft configurations.

Steady and unsteady results were presented for a supersonic fighter configuration to demonstrate application of the Euler solver and dynamic mesh algorithm. The fighter geometry consisted of a high-fineness ratio fuselage with an underslung swept inlet and flow-through duct, a highly swept canard, a cranked wing, and a vertical tail. The steady flow results were obtained for a range of angle of attack. The calculated lift coefficients for the aircraft agreed well with the experimental values. The unsteady flow results were obtained for the aircraft oscillating harmonically in a complete-vehicle bending mode. Effects of angle of attack and reduced frequency on the instantaneous pressures and force responses were shown. The response of the aircraft due to the complete-vehicle bending mode was found to increase with increases in either angle of attack or reduced frequency. The calculated surface-pressure distributions and force coefficient responses demonstrated the capability to compute time-accurate inviscid flows about complex-aircraft configurations undergoing structural deformation.

Finally, the steady and unsteady solutions presented for the Langley fighter required approximately 12×10^6 words of memory and 2 and 6 h CPU time, respectively, on the Cray-2 computer at the Numerical Aerodynamic Simulation facility located at NASA Ames Research Center.

Acknowledgments

The author would like to acknowledge Ken Morgan and Jaime Peraire of the Imperial College of Science, Technology, and Medicine, London, England, for providing the tetrahedral grid for the Langley fighter configuration; and Paresh Parikh of Vigyan Research Associates, Hampton, Virginia, and Rainald Lohner, George Washington University, Washington, D.C., for providing the tetrahedral grid for the Pathfinder 1 configuration. The author would also like to acknowledge the work of Robert W. Neely of Lockheed Engineering and Sciences Company, Hampton, Virginia, in developing the graphics capabilities used in the present study.

References

[1]Jameson, A., "Successes and Challenges in Computational Aerodynamics," AIAA Paper 87-1184, Jan. 1987.

[2]Edwards, J. W., and Thomas, J. L., "Computational Methods for Unsteady Transonic Flows," AIAA Paper 87-0107, Jan. 1987.

[3]Reznick, S. G., and Flores, J., "Strake-Generated Vortex Interactions for a Fighter-Like Configuration," *Journal of Aircraft,* Vol. 26, No. 4, 1989, pp. 289–294.

[4]Flores, J., Chaderjian, N. M., and Sorenson, R. L., "Simulation of Transonic Viscous Flow over a Fighter-Like Configuration Including Inlet," *Journal of Aircraft,* Vol. 26, No. 4, 1989, pp. 295–301.

[5]Jameson, A., and Mavriplis, D. J., "Finite Volume Solution of the Two-Dimensional Euler Equations on a Regular Triangular Mesh," *AIAA Journal*, Vol. 24, No. 4, April 1986, pp. 611–618.

[6]Mavriplis, D. J., "Multigrid Solution of the Two-Dimensional Euler Equations on Unstructured Triangular Meshes," *AIAA Journal,* Vol. 26, No. 6, 1988, pp. 824–831.

[7]Jameson, A., Baker, T. J., and Weatherill, N. P., "Calculation of Inviscid Transonic Flow Over a Complete Aircraft," AIAA Paper 86-0103, Jan. 1986.

[8]Morgan, K., and Peraire, J., "Finite Element Methods for Compressible Flow," Von Karman Institute for Fluid Dynamics Lecture Series 1987-04, Computational Fluid Dynamics, March 1987.

[9]Lohner, R., "Finite Elements in CFD: What Lies Ahead," *International Journal for Numerical Methods in Engineering*, Vol. 24, 1987, pp. 1741–1756.

[10]Morgan, K., Peraire, J., Thareja, R. R., and Stewart, J. R., "An Adaptive Finite Element Scheme for the Euler and Navier-Stokes Equations," AIAA Paper 87-1172, June 1987.

[11]Peraire, J., Peiro, J., Formaggia, L., and Morgan, K., "Finite Element Euler Computations in Three Dimensions," AIAA Paper 88-0032, Jan. 1988.

[12]Batina, J. T., "Unsteady Euler Airfoil Solutions Using Unstructured Dynamic Meshes," AIAA Paper 89-0115, Jan. 1989.

[13]Jameson, A., Schmidt, W., and Turkel, E., "Numerical Solution of the Euler Equations by Finite Volume Methods Using Runge-Kutta Time Stepping Schemes," AIAA Paper 81-1259, June 1981.

[14]Venkatakrishnan, V., "Computation of Unsteady Transonic Flows over Moving Airfoils," Ph.D Dissertation, Princeton University, Princeton, NJ, 1986.

[15]Thomas, P. D., and Lombard, C. K., "Geometric Conservation Law and Its Application to Flow Computations on Moving Grids," *AIAA Journal,* Vol. 17, No. 10, 1979, pp. 1030–1037.

[16]Lohner, R., and Morgan, K., "Finite Element Methods on Supercomputers: The Scatter Problem," *Proceedings of the NUMETA 1985 Conference*, Rotterdam, the Netherlands, 1985, pp. 987–990.

[17]Hom, K. W., and Ticatch, L. A., "Investigation of an Advanced Supersonic Fighter Concept Including Effects of Horizontal Tail and Canard Control Surfaces over a Mach Number Range From 1.6 to 2.5," NASA TP-2526, May 1986.